

Use of local-density approximation pseudopotentials in range separated hybrid exchange-correlation functional method to investigate Pb doped SnO₂

Veysel Çelik^{1,*}

¹*Department of Mathematics and Science Education, Siirt University, Siirt 56100, Turkey*
(Dated: October 30, 2020)

In this study, the structural, electronic and optical properties of Pb doped rutile SnO₂ were investigated using the range separated hybrid exchange-correlation functional method. In the calculations, LDA pseudopotentials were used instead of the standard PBE pseudopotentials. According to the results obtained in this present work, when the LDA pseudopotentials are used instead of PBE pseudopotentials in HSE06 method with a mixing parameter of %29, the electronic structure of rutile SnO₂ can be described as quite compatible with experimental data. At the same time, in the Pb doped SnO₂ cases, using the same method, electronic structure, and especially the band gap were described quite compatible with the experimental data. Consistent with experimental data, the band gap narrows as the Pb doping rate increases. The computational results obtained in this study show that the reason for this narrowing is the change in the conduction band edges. Due to this effect of the Pb atom, the bandgap can be narrowed in a controlled manner by using the addition amount of the Pb atom.

PACS numbers: 68.43.Bc, 68.43.Fg

I. INTRODUCTION

Due to its combination of high electrical conductivity and optical transparency, transparent conductive oxides (TCO) are important for solar cell.^{1,2} Among the TCO materials, tin dioxide (SnO₂) has excellent electrical, optical and electro-chemical properties. Tin dioxides have been widely used for solar panels^{3,4} and touch screens.⁵ The SnO₂ is efficient electron Transport Layer for Perovskite Solar Cells.² For these mentioned applications, it is important to be able to adjust the bandgap that SnO₂ has. The photocatalytic activity can be adjusted by changing the band gap. The SnO₂ has a direct band gap whose width is about 3.6 eV (Ref. 6) which is in the ultraviolet region. The ultraviolet region is a small fraction of the solar spectrum compared to the visible region. Under the sunlight, if we want to increase the photocatalytic activity of the SnO₂, we must facilitate the transition of electrons excited by the photon of the visible region, from the valence band into the conduction band. Narrowing the band gap may provide this.

Many experimental studies have been conducted on how the structural, electronic and optical properties of SnO₂ have changed when it is doped with impurity atoms.⁷⁻¹⁷ The Ni doping rate of %9 narrows the band gap from 3.90 eV to 3.31 eV and shortens the lattice parameters according to the pure case.¹³ In case of doping with Mn, the band gap expands as the doping rate increases, and with %15 the band gap increases from 3.71 eV to 4 eV.¹⁴ In case of Cu doping, the bandwidth expands from 3.93 eV to 4.00 eV, with a %5 doping rate.⁷ On the other hand, the Cu-doped SnO₂ quantum dots samples exhibited enhanced absorption capability in the visible light region and the band gap decreased to about 2.2 eV by the increasing concentration of Cu.¹⁸ In the experimental study with Pb doping, it was found that the %15 doping rate narrowed the bandwidth from 3.64 eV

to 2.87 eV.¹⁹ On the other hand, in the density functional theory (DFT) frame, many studies have been carried out on the changes in the structural and electronic properties of impurity-doped SnO₂.⁸⁻¹² The general problem in theoretical studies is to calculate the band gap closer to the experimental data. This is one of the focal points in this study. On the other hand, there is a lack of theoretical investigation in the literature regarding Pb doped SnO₂.

In this study, structural, electronic and optical properties of Pb doped SnO₂ were investigated. Pb is in the same group as Sn and has a larger ionic radius. In this present work, screened Coulomb potential hybrid DFT calculations was used to investigate the modifications of the electronic properties of SnO₂ induced by one Pb doping (Pb₁), two Pb doping (Pb₂) and three Pb doping (Pb₃) cases and their effects on the corresponding imaginary part of the dielectric constant. Formation energies have been calculated as a function of oxygen chemical potential to compare thermodynamical stability of the doped structures.

II. COMPUTATIONAL METHOD

The spin-polarized hybrid density functional theory (DFT) calculations have been performed based on the projector-augmented wave (PAW)^{20,21} method as implemented in the Vienna ab-initio simulation package (VASP).^{22,23} The exchange-correlation effects have been taken into account by employing the range separated hybrid HSE functional.^{24,25} In the calculations, the pseudopotentials in the Local Density Approach (LDA)^{23,26,27} framework were used. The Sn potential which treats the 4d semicore states as valence states were used for bulk rutile SnO₂ calculation. On the other hand, due to the high computational cost, the potential that treats the 4d semicore states as core states was used in

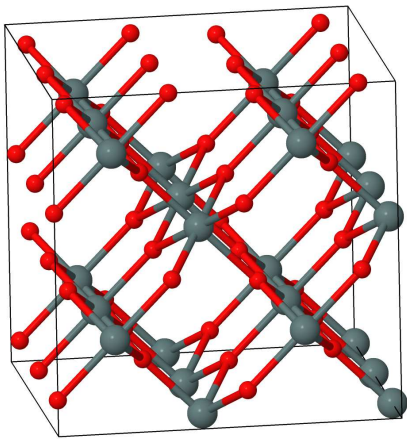


FIG. 1. $\text{Sn}_{24}\text{O}_{48}$ supercell. Red small and large gray balls presented O and Sn, respectively.

the doping case calculations. According to the tests performed in this study, using these two types of potentials in HSE calculation gives similar results for the structure of VB, CB and crystal.

The lack of a proper self-interaction correction (SIC) leads to the well-known band gap underestimation by the standard DFT exchange-correlation functionals, such as Perdew–Burke–Ernzerhof exchange-correlation functional (PBE).²⁸ On the other hand, Hartree-Fock (HF) formalism has well-defined Coulomb direct and exchange terms canceling each other for the zero momentum components avoiding self-interaction of charges. In order to benefit from this, modern hybrid DFT functionals partially admix the nonlocal exact exchange energy with the semilocal PBE exchange energy.

The hybrid HSE functional treats the exchange energy as composed of long-range (LR) and short-range (SR) parts with a range separation parameter ω and mixes the exact exchange with the PBE exchange at the short-range by a mixing factor of $a = 0.25$ such that,^{24,25}

$$E_{\mathbf{x}}^{\text{HSE}} = aE_{\mathbf{x}}^{\text{HF,SR}}(\omega) + (1-a)E_{\mathbf{x}}^{\text{PBE,SR}}(\omega) + E_{\mathbf{x}}^{\text{PBE,LR}}(\omega).$$

The correlation term of the XC energy is taken from standard PBE correlation energy.²⁸ However, in this present work, with the same formula, hybrid functional mix local exchange potentials in the LDA with the exact nonlocal Hartree–Fock exchange potential. At the same time, the correlation energy is described within the LDA. The exact exchange contribution was determined to take into account the experimental data. In this context, the exact exchange contribution of %29 described closest to experimental band gap value of SnO_2 for the rutile phase. This rate is close to the standard rate of %25.

In this work, 72-atom rutile bulk supercell containing 24 Sn atoms and 48 O atoms used for doped systems, as shown in Fig. 1. Supercells arised from $2 \times 2 \times 3$ replication of the rutile unit cell of SnO_2 . The Pb atom was substituted for Sn atoms. For geometry optimizations and electronic-structure, the Brillouin zones were

sampled with $2 \times 2 \times 2$ Monkhorst-Pack²⁹ k -point grids for 72 atoms supercells. Plane wave basis set was used to expand the wavefunctions up to a kinetic energy cutoff value of 450 eV. The fine FFT grids with high precision settings were used throughout the calculations. Atomic positions and cell parameters were optimized until residual forces were below 0.01 eV/Å.

For the qualitative description of interatomic charge distributions, Bader analysis based on atom in molecule (AIM) theory used. Local charge depletion/accumulation can be computed by integrating Bader volumes around atomic sites. These volumes are partitions of the real space cell delimited by local zero-flux surfaces of charge density gradient vector field. Charge states of atomic species (see Table II) were calculated using a grid based decomposition algorithm developed by Henkelman’s group.³⁰

TABLE I. The comparison of computational and experimental data for rutile bulk SnO_2 . Lattice parameters and band gaps are in angstroms and eV, respectively.

Functional	Lattice parameters (Å)		Band gaps (eV)
	a	c	
LDA ^a	4.73	3.20	1.08
GGA ^b	4.83	3.24	0.65
GGA+U(4 eV) ^c	4.73	3.16	1.93
HSE06 ^d	4.76	3.19	2.96
HSE03+G ₀ W ₀ ^a	-	-	3.65
This Work	4.70	3.16	3.60
Experimental	4.73 ^e	3.18 ^e	3.60 ^f

^a Reference 31.

^b Reference 32.

^c Reference 33.

^d Reference 34.

^e Reference 35.

^f Reference 6.

TABLE II. Average charge states (e) of dopants and their adjacent Sn and O atoms from Bader analysis.

Structure	Pure	Pb ₁	Pb ₂	Pb ₃
Sn _{<i>n</i>1}	+2.42	+2.41	+2.42	+2.42
Sn _{<i>n</i>2}	+2.42	+2.40	+2.41	+2.42
O _{<i>n</i>1}	-1.20	-1.14	-1.14	-1.15
O _{<i>n</i>2}	-1.20	-1.14	-1.14	-1.13
O _{<i>nn</i>}	-	-	-1.06	-1.06
Pb ₁₁	-	+2.01	-	-
Pb ₂₁	-	-	+2.02	-
Pb ₂₂	-	-	+1.96	-
Pb ₃₁	-	-	-	+1.98
Pb ₃₂	-	-	-	+2.02
Pb ₃₃	-	-	-	+2.01

III. RESULTS & DISCUSSION

Previous theoretical studies show that HSE functional is useful to get electronic band gap related features of periodic and finite physical systems reasonably accurate to be comparable with experiments.³⁶⁻³⁸ However, for rutile SnO₂, in the calculations made by HSE06 method, which were used the default %25 mixing rate, the bandgap was calculated 2.96 eV (Ref. 34). This value is less than the experimental value of 3.6 eV (Ref. 6). Behtash *et al.*³⁹, Increased the mix ratio to 33 percent to approximate the experimental band gap value in the HSE06 calculation. In another study, using first-order perturbation theory based on an initial electronic structure from HSE03, the bandgap was calculated 3.65 eV.³¹ As an alternative method, in this present work, with a %29 mixing rate, the calculated value for the band gap is 3.60 eV. The obtained DOS pattern for bulk rutile SnO₂ is shown in Fig 2. The averaged d states is located 21.1 eV below the valence band maximum (VBM), which is good agreement with the reported experimental values of 21.1 eV (Ref. 40) and 21.5 eV (Ref. 41). The PBE and LDA calculations underestimate the binding energy of the averaged d states and their positions are 19.9 eV and 19.7 eV below the VBM for PBE and LDA, respectively. As can be seen in Fig. 2, the calculated valence band (VB) width is 8.7 eV and this value is close to the experimental value of 8.5 eV from resonant photoelectron spectroscopy.⁴² In the VB, O p energy levels are dominant. There are Sn d energy levels below the top of the VB. In the lower parts of the conduction band (CB), Sn s-O p energy levels are dominant. The characteristics of the electronic structure obtained with the calculations made in this study are compatible with the standard DFT and hybrid DFT studies that have been done before.^{31,39,43-46} By comparison, LDA can describe rutile SnO₂ better than GGA-PBE. One of the aims of this present work is to use this

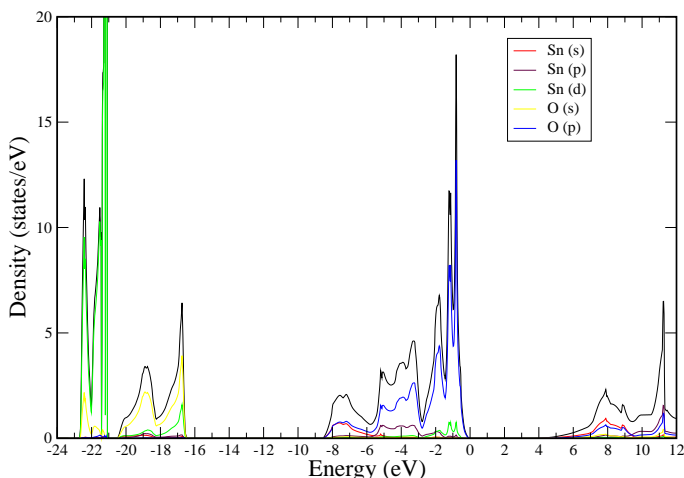


FIG. 2. Densities of states (DOS) of bulk rutile SnO₂.

In terms of structural features, lattice parameters can be calculated very close to experimental value with LDA functional, but relatively higher with GGA-PBE functional (See Table I). With the default mixing parameter of %25 in HSE functional, by correcting the overestimate in the calculation made with GGA-PBE functional, the lattice parameters can be calculated close to the experimental value, but, on the other side, the value of the band gap is calculated lower than it should be. In this present work, calculated lattice parameters are $a = 4.70 \text{ \AA}$ and $c = 3.16 \text{ \AA}$, which are slightly underestimate compared with the experimental values³⁵ ($a = 4.73 \text{ \AA}$ and $c = 3.18 \text{ \AA}$). As mentioned earlier, using standard LDA, the lattice parameter can be calculated very close to experimental data. Increasing the amount of the exact exchange contribution causes the lattice parameter to shorten while expanding the bandgap. However, these calculated values are acceptable.

In this work, the dopant formation energies have been calculated using,

$$E_f = E_{\text{doped}} - E_{\text{pure}} - n\mu_{\text{Pb}} + n\mu_{\text{Sn}},$$

where E_{doped} and E_{pure} are the total energies of doped and pure supercells, while μ_{Pb} and μ_{Sn} are the chemical potentials of the Pb and Sn species, respectively. The integer n gives the number of Pb cations. In thermodynamical equilibrium with the rutile phase, μ_{Sn} and μ_{O} must satisfy the relation $\mu_{\text{SnO}_2} = \mu_{\text{Sn}} + 2\mu_{\text{O}}$. The amount of Sn and O in a growth environment influences their chemical potentials. High(low) values of μ_{O} correspond to O-rich(-poor) conditions and can also be interpreted as Sn-poor(-rich) conditions from the equilibrium relation. Under O-rich conditions, μ_{O} is the half of the energy of an O₂ molecule (E_{O_2}), and μ_{Sn} is obtained through the condition $\mu_{\text{Sn}} = \mu_{\text{SnO}_2} - E_{\text{O}_2}$. Under Sn-rich conditions, μ_{Sn} is the energy of a Sn atom in its bulk unit cell ($\mu_{\text{Sn}}^{\text{bulk}}$) and μ_{O} is calculated from the equilibrium restriction by $\mu_{\text{O}} = \frac{1}{2}(\mu_{\text{SnO}_2} - \mu_{\text{Sn}})$. The chemical potentials of the dopants are extracted from their naturally occurring phases. μ_{Pb} is the energy of a Pb atom in its bulk unit cell ($\mu_{\text{Pb}}^{\text{bulk}}$). Calculated dopant formation energies are given in Fig. 8. In this study, the formation enthalpy calculated for bulk rutile SnO₂ is -6.1 eV and this value is very close to the experimental value of about -6.0 eV (Ref. 48).

TABLE III. Comparison of the computational result of the band gaps according to the doping cases. The band gap energies are in eV.

Structure	Band Gap (eV)	Transition
Pure	3.60	$\Gamma \rightarrow \Gamma$
Pb ₁	3.39	$\Gamma \rightarrow \Gamma$
Pb ₂	3.17	$\Gamma \rightarrow \Gamma$
Pb ₃	3.02	$\Gamma \rightarrow \Gamma$

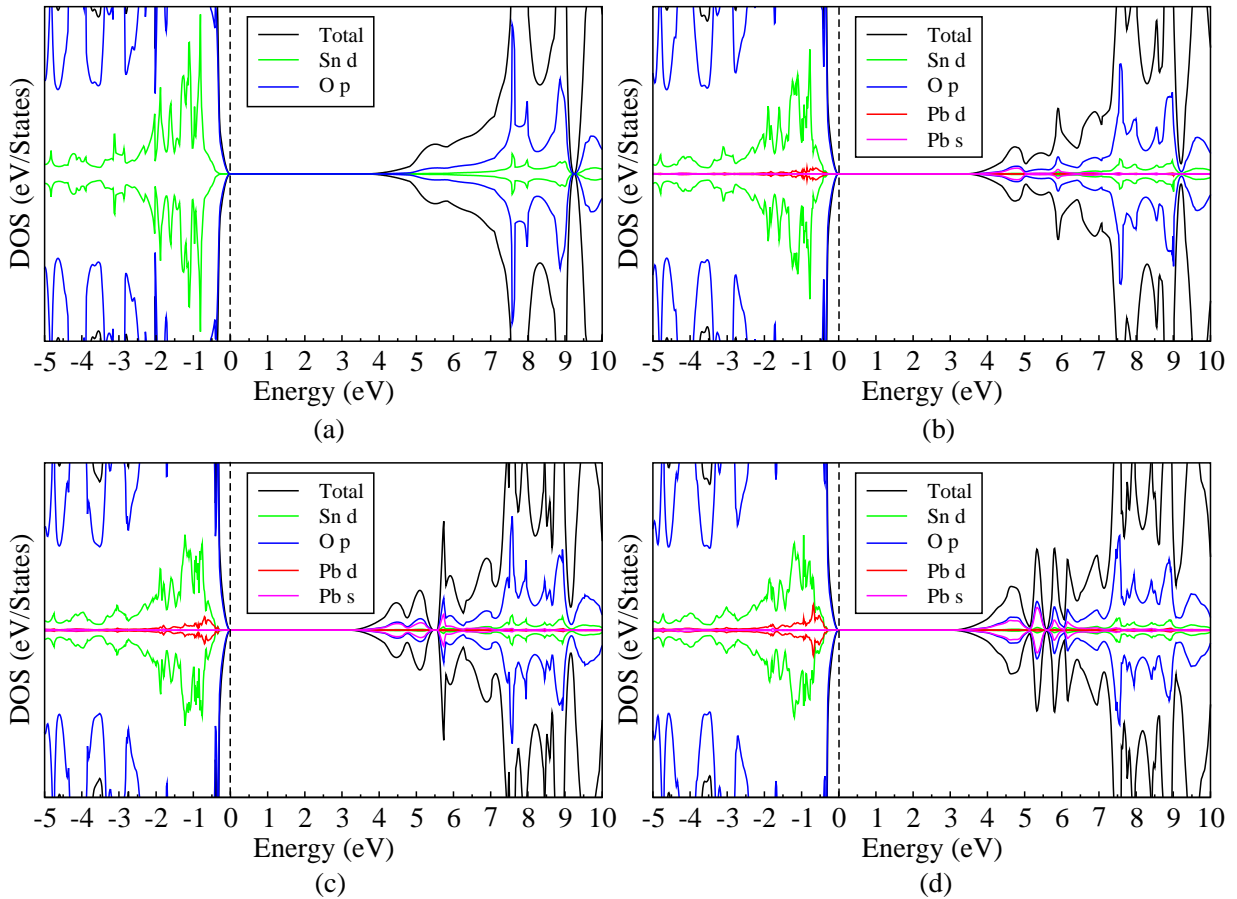


FIG. 3. Densities of states (DOS) of (a) pure, (b) Pb_1 , (c) Pb_2 and (d) Pb_3 structures. Dotted line indicates the Fermi energy.

One Pb doping (Pb_1): According to the calculations in this study, in accordance with experimental data,¹⁹ it is more convenient to replace the Pb atom with an Sn atom in terms of energy. In this structure, there are 6 adjacent O atoms to a Pb atom. As will be seen in Fig. 4, the bond length of these 6 oxygen atoms with the Pb atom is 2.13Å for the 4 cross-located oxygen atoms and 2.10Å for the other 2 oxygen atoms. For Sn atoms shown in Fig. 4, the bond length between Sn and O atoms was calculated as about 2.02Å in the Pb doped SnO_2 . In pure SnO_2 , the Sn-O bond length is 2.03Å. There is no noticeable change in Sn-O bond length compared to the pure case. Since Pb atom has a larger ionic radius than Sn atom, the Pb atom pushes the adjacent O atoms outward in a small amount. At the same time, the angle between the O atoms in the O-Sn-O chain opens according to the pure case so that the Sn-O bond lengths do not change much. Pb doping does not distort the crystal structure considerably, and the distortion that occurs is local. This result is consistent with the X-ray diffraction results obtained in an experimental study.¹⁹

The density of states (DOS) plots in Fig. 3(b) show the electronic structure of the single Pb doping. Impurity incorporation hasn't induced a local empty state in the energy gap between the VB and the CB. The clearance

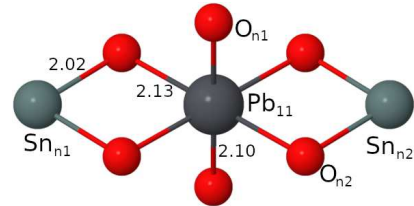


FIG. 4. Relaxed structure of the one Pb dopant inside the rutile SnO_2 . The Bond lengths are in angstroms.

of the bandgap indicates that there are no electron traps in the bandgap. The electron traps can increase the possibility of electron-hole recombination before the electron is transferred to the conduction band. As can be seen in Table III, the band gap is direct ($\Gamma \rightarrow \Gamma$) and has a width of 3.39 eV. According to the pure case, single Pb doping narrows the band gap. The imaginary parts of dielectric constant values versus photon energy of Pb doped SnO_2 with different doping levels are shown in Fig. 5. The imaginary part (ϵ_2) of the dielectric constant depends mainly on the coefficient of extinction, which depends on the variation of the absorption coefficient. In this way, as can be seen in Fig 5, Pb doping leads to redshift in the

imaginary parts of dielectric constant, which is consistent with the electronic band structure. The single Pb doping doesn't lead to much change in the VB edges, but considerably changes the formation of the CB bottom edges. The computational results revealed that the general reason for the narrowing of the bandgap is the formation in the CB bottom edges where Pb 6s-O 2p empty energy states are dominant (see Fig. 3(b)). In pure SnO₂, Sn 5s-O 2p hybrid energy states are dominant in the lower parts of the CB. When Pb and Sn are replaced, Pb-O bonds are formed. In these bonds, Pb 6s energy levels replace Sn 5s and Pb 6s-O 2p hybrid energy levels form. The Pb 6s energy levels are pushing the CB bottom edges towards the band gap. Moreover, looking at the charge distributions of atoms in Table II, the charges around the Pb atom are approximately 0.40e more than Sn atom. At the same time, the charge of each of the O atoms bonding with the Pb atom is about 0.06e less than in the pure case. A possible reason is that the Pb atom having a larger ionic radius than the Sn atom, and

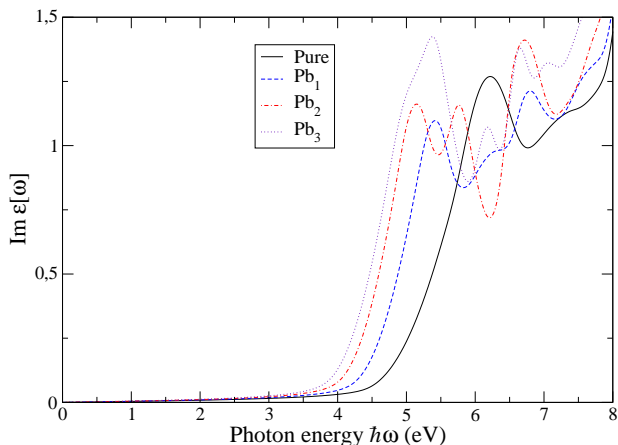


FIG. 5. The imaginary part of dielectric function for pure, Pb₁, Pb₂ and Pb₃ structures.

Two Pb doping (Pb₂): The energies of various combinations were compared to find the most stable configuration of the two Pb doped SnO₂ (see Fig. 6). The adding of two Pb atoms into the 72-atom supercell corresponds to the impurity doping rate of %8.33. The measured distance between the two Pb atoms in the supercell is 3.74Å, as will be seen in Fig. 6. Similar to that of a single Pb doping, the bond length between the Pb and the O atoms is about 2.13Å. As can be seen in the calculated formation energies in Fig. 8, the energy of Pb₂ in the O-poor environment is lower than Pb₃ and higher than Pb₁, whereas in the O-rich environment the energy is lower than Pb₁ and higher than Pb₃.

In terms of electronic structure, as can be seen in Fig 3(c), there is no noticeable change in the shape of the VB edges. The Pb d energy states are located below the VB edge and their density increases with the addition of the second Pb compared to the Pb₁ case. In the VB edges

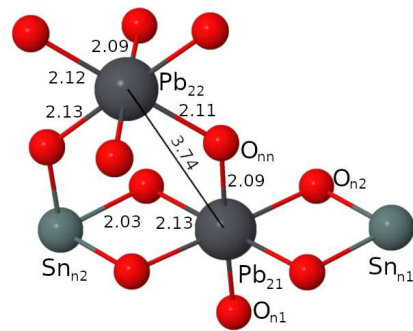


FIG. 6. Relaxed structure of the two Pb dopant inside the rutile SnO₂. The Bond lengths are in angstroms.

O p Energy levels are dominant. On the other hand, changes occur in the CB band edge and the empty energy states start from 0.45 eV lower than the pure case. Where, unlike Pb₁, empty energy states occur about 0.1 eV below the CB. The O_{nn} (See Fig. 6) atom which is bonded with two Pb atoms is dominant in first peak at the bottom of these separate energy states and its charge is 0.08e less than other O atoms bonded with Pb (See Table II). The O atoms that bond with the Pb atom are dominant in the lower parts of the CB. As a result of these formations in the CB edge, the bandgap narrows to 3.19 eV, and the transitions are direct ($\Gamma \rightarrow \Gamma$). The changes in the edge of the CB are effective in the narrowing here. This narrowing is consistent with redshifting in the imaginary parts of the dielectric constant and that is more than in Pb₁ case (See Fig. 5). The structural and electronic properties of the double Pb doping shows similar characteristics with the one defect case, which indicates that the defect-defect interaction is weak due to the distance between the Pb atoms.

Three Pb doping (Pb₃): The adding of three Pb atoms into the 72-atom supercell corresponds to the impurity doping rate of %12.5. To find the most stable configuration of the triple Pb doping, various interatomic distances between dopants were tested by comparing the

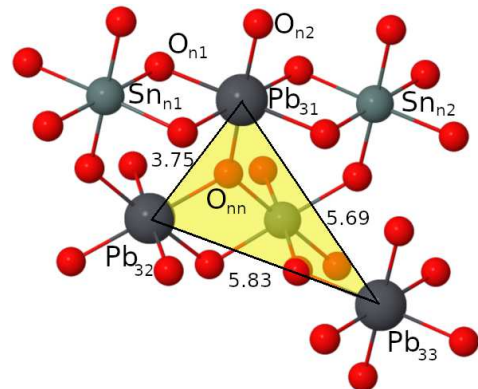


FIG. 7. Relaxed structure of the three Pb dopant inside the rutile SnO₂. The Bond lengths are in angstroms.

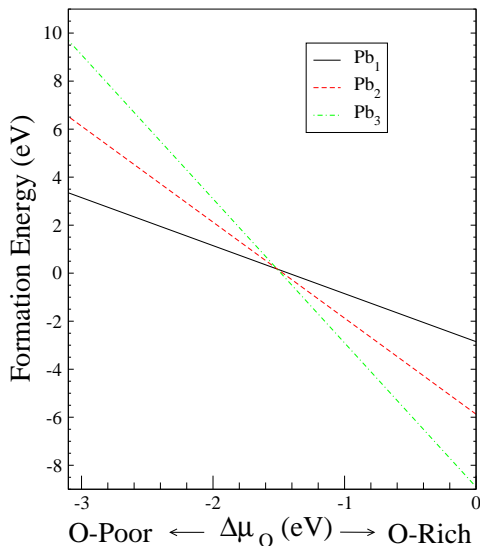


FIG. 8. Calculated formation energies as a function of the oxygen chemical potential for Pb₁, Pb₂ and Pb₃ structures.

energies. Considering that the distances between Pb atoms form a triangle, as shown in Fig. 7, the lengths of Pb₃₃-Pb₃₁, Pb₃₃-Pb₃₂ and Pb₃₁-Pb₃₂ are 5.69Å, 5.83Å and 3.75Å, respectively. According to this structure, the third Pb atom prefers to be located farther away from the other two Pb atoms. As with the Pb₂ case, dopants do not tend to make a cluster. When the amount of Pb in the supercell increases, elongation occurs in the lattice parameters. In Pb₃ case, this elongation is 0.02Å and 0.023Å for *a* and *c*, respectively. These values are in good agreement with the experimental data.¹⁹ As shown in Fig. 8, the calculated formation energies of the three Pb doping under O-rich and O-poor conditions are -8.71 eV and 9.61 eV, respectively. Calculated formation energies show that under O-rich conditions, the three Pb doping are energetically more favorable than the others and vice versa under the O-poor conditions.

As can be seen in Table III, the calculation results show that with the impurity doping rate of %12.5, the band gap of SnO₂ is direct ($\Gamma \rightarrow \Gamma$) and has a width of 3.02 eV. In an experimental study, Sarangi *et al.*¹⁹ show that a %15 Pb doping narrows the band gap of SnO₂ to 2.98 eV. Considering that the narrowing in the band gap is proportional to the doping rate, the computational result is in good agreement with the experimental data. The band gap narrowing in Pb₃ case is higher than the Pb₁ and Pb₂ cases. In agreement with the experimental data, as the number of Pb increases, the band gap narrows. This feature can be used to fine-tune the width of the band gap. The obtained DOS pattern for Pb₃ case is shown in Fig. 3(d). As can be seen from the DOS

pattern, there are no energy levels induced by dopants in the band gap. The VB band edges show similar characteristics to Pb₁ and Pb₂, and the Pb d energy levels density in VB is more than Pb₁ and Pb₂. As can be seen from the DOS pattern (see Fig. 3(d)), in the case of Pb₃, as in Pb₁ and Pb₂, the narrowing of the bandgap is caused by the formation of the bottom of CB, where Pb 6s-O 2p hybrid states predominate. Pb 6s-O_{nn} 2p empty energy levels predominate in the first peak at the bottom of the CB. In the other two peaks, as in Pb₂ case, empty Pb s-O 2p hybrid energy levels induced by the other O atoms bonded with Pb predominate. As can be seen in Fig. 3(d), the addition of the third Pb atom causes the closure of the 0.1 eV wide gap between the second and third peaks in the case of Pb₂. At the same time, in the case of Pb₃, with the increase in the density of the peaks compared to other cases, three more intense Pb 6s-O 2p hybrid empty energy levels are formed at the bottom of the CB. In the imaginary part of the dielectric constant (see Fig. 5), there is a redshift that compatible with the narrowing of the band gap and this shifting is more than in the other cases. However, compared to other cases, the formed shoulder is higher and wider. The formation that occurs at the bottom of CB is effective in the formation of this shoulder. This result indicates that the photocatalytic activity of the Pb₃ case stronger in the visible region than in the other cases.

IV. CONCLUSION

According to the results obtained in this present work, when the LDA pseudopotentials are used instead of PBE pseudopotentials in HSE06 method with a mixing parameter of %29, the electronic structure of rutile SnO₂ can be described as quite compatible with experimental data. On the other hand, in the Pb doped SnO₂ cases, using the same method, electronic structure, and especially the band gap were calculated quite compatible with the experimental data. Consistent with experimental data, the band gap narrows as the Pb doping rate increases. The computational results obtained in this study show that the reason for this narrowing is the change in the conduction band edges. The Pb 6s energy levels are pushing the CB bottom edges towards the band gap. On the other hand, the narrowing in the band gap is not based on structural distortion, as Pb doping does not significantly distort the structure. Due to this effect of the Pb atom, the bandgap can be narrowed in a controlled manner by using the addition amount of the Pb atom. Although the increase in the amount of Pb and the narrowing of the band gap is proportional, the rate of increase of photocatalytic activity in the visible region is higher in the case of Pb₃ than in the other cases.

* veysel3@gmail.com

¹ A. Klein, C. Körber, A. Wachau, F. Säuberlich, Y. Gassenbauer, S. P. Harvey, D. E. Proffit, and T. O. Mason, [Ma-](#)

- terials **3**, 4892 (2010).
- ² Q. Jiang, X. Zhang, and J. You, *Small* **14**, 1801154 (2018).
 - ³ Q. Jiang, L. Zhang, H. Wang, X. Yang, J. Meng, H. Liu, Z. Yin, J. Wu, X. Zhang, and J. You, *Nature Energy* **2**, 16177 EP (2016).
 - ⁴ K. Ellmer, *Nature Photonics* **6**, 809 EP (2012), review Article.
 - ⁵ N. Kikuchi, E. Kusano, E. Kishio, and A. Kinbara, *Vacuum* **66**, 365 (2002), selected Papers revised from the Proceedings of the Sixth International Symposium on Sputtering and Plasma Processes (ISSP 2001) 13-15 June 2001, Japan.
 - ⁶ K. G. Godinho, A. Walsh, and G. W. Watson, *The Journal of Physical Chemistry C* **113**, 439 (2009).
 - ⁷ P. Chetri, B. Saikia, and A. Choudhury, *Journal of Applied Physics* **113**, 233514 (2013).
 - ⁸ W. Chen and J. Li, *Journal of Applied Physics* **109**, 083930 (2011).
 - ⁹ H. Wang, Y. Yan, Y. S. Mohammed, X. Du, K. Li, and H. Jin, *Journal of Magnetism and Magnetic Materials* **321**, 3114 (2009).
 - ¹⁰ C. G. Van de Walle and A. Janotti, *physica status solidi (b)* **248** (2011), 10.1002/pssb.201190000.
 - ¹¹ W.-Z. Xiao, L.-L. Wang, L. Xu, Q. Wan, and B. Zou, *Solid State Communications* **149**, 1304 (2009).
 - ¹² A. F. Lamrani, M. Belaiche, A. Benyoussef, A. E. Kenz, and E. Saidi, *Journal of Magnetism and Magnetic Materials* **323**, 2982 (2011).
 - ¹³ A. S. Ahmed, M. S. M.], M. Singla, S. Tabassum, A. H. Naqvi, and A. Azam, *Journal of Luminescence* **131**, 1 (2011).
 - ¹⁴ A. Azam, A. S. Ahmed, S. S. Habib, and A. Naqvi, *Journal of Alloys and Compounds* **523**, 83 (2012).
 - ¹⁵ R. Adhikari, A. K. Das, D. Karmakar, T. V. C. Rao, and J. Ghatak, *Phys. Rev. B* **78**, 024404 (2008).
 - ¹⁶ A. Bouaine, N. Brihi, G. Schmerber, C. Ulhaq-Bouillet, S. Colis, and A. Dinia, *The Journal of Physical Chemistry C* **111**, 2924 (2007).
 - ¹⁷ J. Hays, A. Punnoose, R. Baldner, M. H. Engelhard, J. Peloquin, and K. M. Reddy, *Phys. Rev. B* **72**, 075203 (2005).
 - ¹⁸ B. Babu, A. Kadam, R. Ravikumar, and C. Byon, *Journal of Alloys and Compounds* **703**, 330 (2017).
 - ¹⁹ S. Sarangi, G. K. Pradhan, and D. Samal, *Journal of Alloys and Compounds* **762**, 16 (2018).
 - ²⁰ P. E. Blöchl, *Phys. Rev. B* **50**, 17953 (1994).
 - ²¹ G. Kresse and J. Furthmüller, *Phys. Rev. B* **54**, 11169 (1996).
 - ²² G. Kresse and J. Hafner, *Phys. Rev. B* **47**, 558 (1993).
 - ²³ G. Kresse and D. Joubert, *Phys. Rev. B* **59**, 1758 (1999).
 - ²⁴ J. Heyd, G. E. Scuseria, and M. Ernzerhof, *The Journal of Chemical Physics* **118**, 8207 (2003).
 - ²⁵ J. Paier, M. Marsman, K. Hummer, G. Kresse, I. C. Gerber, and J. G. Ángyán, *The Journal of Chemical Physics* **124**, 154709 (2006).
 - ²⁶ W. Kohn and L. J. Sham, *Phys. Rev.* **140**, A1133 (1965).
 - ²⁷ D. M. Ceperley and B. J. Alder, *Phys. Rev. Lett.* **45**, 566 (1980).
 - ²⁸ J. P. Perdew, K. Burke, and M. Ernzerhof, *Phys. Rev. Lett.* **77**, 3865 (1996).
 - ²⁹ H. J. Monkhorst and J. D. Pack, *Phys. Rev. B* **13**, 5188 (1976).
 - ³⁰ W. Tang, E. Sanville, and G. Henkelman, *Journal of Physics: Condensed Matter* **21**, 084204 (2009).
 - ³¹ A. Schleife, J. B. Varley, F. Fuchs, C. Rödl, F. Bechstedt, P. Rinke, A. Janotti, and C. G. Van de Walle, *Phys. Rev. B* **83**, 035116 (2011).
 - ³² P. D. Borges, L. M. R. Scolfaro, H. W. Leite Alves, and E. F. da Silva, *Theoretical Chemistry Accounts* **126**, 39 (2010).
 - ³³ A. Stashans, P. Puchaicela, and R. Rivera, *Journal of Materials Science* **49**, 2904 (2014).
 - ³⁴ J. B. Varley, A. Janotti, A. K. Singh, and C. G. Van de Walle, *Phys. Rev. B* **79**, 245206 (2009).
 - ³⁵ A. A. Bolzan, C. Fong, B. J. Kennedy, and C. J. Howard, *Acta Crystallographica Section B* **53**, 373 (1997).
 - ³⁶ T. M. Henderson, J. Paier, and G. E. Scuseria, *physica status solidi (b)* **248**, 767 (2011).
 - ³⁷ V. Çelik and E. Mete, *Phys. Rev. B* **86**, 205112 (2012).
 - ³⁸ F. Viñes, O. Lamiel-García, K. Chul Ko, J. Yong Lee, and F. Illas, *Journal of Computational Chemistry* **38**, 781 (2017).
 - ³⁹ M. Behtash, P. H. Joo, S. Nazir, and K. Yang, *Journal of Applied Physics* **117**, 175101 (2015).
 - ⁴⁰ P. M. A. Sherwood, *Phys. Rev. B* **41**, 10151 (1990).
 - ⁴¹ J.-M. Themlin, M. Chtaïb, L. Henrard, P. Lambin, J. Darville, and J.-M. Gilles, *Phys. Rev. B* **46**, 2460 (1992).
 - ⁴² J. Haeberle, S. Machulik, C. Janowitz, R. Manzke, D. Gaspar, P. Barquinha, and D. Schmeißer, *Journal of Applied Physics* **120**, 105101 (2016).
 - ⁴³ Y. Duan, *Phys. Rev. B* **77**, 045332 (2008).
 - ⁴⁴ K. C. Mishra, K. H. Johnson, and P. C. Schmidt, *Phys. Rev. B* **51**, 13972 (1995).
 - ⁴⁵ V. Zainullina, *Physica B: Condensed Matter* **391**, 280 (2007).
 - ⁴⁶ B. A. Hamad, *The European Physical Journal B* **70**, 163 (2009).
 - ⁴⁷ J. B. Varley, A. Janotti, and C. G. Van de Walle, *Phys. Rev. B* **81**, 245216 (2010).
 - ⁴⁸ D. R. Lide, *CRC Handbook of Chemistry and Physics, 2009-2010, 90th ed.*, 90th ed., Vol. 1 (CRC Press, Boca Raton, Florida, 2009).